






The human GID complex engages two independent modules for substrate recruitment

Weaam I Mohamed¹ , Sophia L Park^{1,2,†} , Julius Rabi^{3,†} , Alexander Leitner⁴ , Daniel Boehringer³ & Matthias Peter^{1,*} 

Abstract

The human GID (hGID) complex is a conserved E3 ubiquitin ligase regulating diverse biological processes, including glucose metabolism and cell cycle progression. However, the biochemical function and substrate recognition of the multi-subunit complex remain poorly understood. Using biochemical assays, cross-linking mass spectrometry, and cryo-electron microscopy, we show that hGID engages two distinct modules for substrate recruitment, dependent on either WDR26 or GID4. WDR26 and RanBP9 cooperate to ubiquitinate HBP1 *in vitro*, while GID4 is dispensable for this reaction. In contrast, GID4 functions as an adaptor for the substrate ZMYND19, which surprisingly lacks a Pro/N-end degron. GID4 substrate binding and ligase activity is regulated by ARMC8 α , while the shorter ARMC8 β isoform assembles into a stable hGID complex that is unable to recruit GID4. Cryo-EM reconstructions of these hGID complexes reveal the localization of WDR26 within a ring-like, tetrameric architecture and suggest that GID4 and WDR26/Gid7 utilize different, non-overlapping binding sites. Together, these data advance our mechanistic understanding of how the hGID complex recruits cognate substrates and provides insights into the regulation of its E3 ligase activity.

Keywords E3 ligase; hGID/CTLH; oligomerization; substrate receptors; ubiquitin

Subject Categories Post-translational Modifications & Proteolysis; Structural Biology

DOI 10.15252/embr.202152981 | Received 1 April 2021 | Revised 31 August 2021 | Accepted 8 September 2021 | Published online 14 October 2021

EMBO Reports (2021) 22: e52981

Introduction

The ubiquitin-proteasome system (UPS) is required for cells to adjust to different nutrient conditions, such as limiting carbon sources. Changing metabolic flux is often controlled by regulating the relative abundance of rate-limiting enzymes that function in distinct exergonic pathways (Nakatsukasa *et al*, 2015). In yeast,

gluconeogenesis and glycolysis are intermittently coordinated to prevent simultaneous glucose production and break-down. This is achieved in part by the glucose-induced deficient degradation (GID) complex (Santt *et al*, 2008), a multi-subunit E3 ligase that specifically targets the surplus of gluconeogenic enzymes for proteasomal degradation, including the conserved fructose-1,6-bisphosphatase 1 (Fbp1) in yeast. Adequate glucose levels induce expression of its critical subunit Gid4 (Santt *et al*, 2008), which is otherwise degraded by autoubiquitination. Interestingly, Gid4 functions as a substrate receptor recognizing a Pro/N-end degron motif (Chen, 2017; Dong *et al*, 2018; Qiao *et al*, 2019). Gid4 is partially redundant with Gid10, which is upregulated by heat and osmotic stress conditions (Melnykov *et al*, 2019; Qiao *et al*, 2019). Moreover, Gid11/Ylr149c was recently identified as a GID substrate receptor recognizing proteins with N-terminal threonine residues (Kong *et al*, 2021), thus expanding the specificity of the GID complex. Interestingly, these substrate receptors are recruited to the GID complex by binding to Gid5, which, in turn, interacts with the catalytic core composed of Gid8 and the RING domain-containing subunits Gid2 and Gid9. Structural analysis of the monomeric GID complex also identified an essential role of Gid1, which interacts with Gid8 and Gid5. In contrast to these subunits, Gid7 is not required to degrade gluconeogenic enzymes (Menssen *et al*, 2018). Indeed, Gid7 does not stably incorporate into the monomeric yeast GID complex (Qiao *et al*, 2019), and the role of Gid7 thus remains unclear.

Interestingly, the GID E3 ligase complex is highly conserved, and all seven yeast GID subunits have homologous counterparts in humans. RanBP9 (Gid1), RMND5a (Gid2), ARMC8 (Gid5), TWA1 (Gid8), and MAEA (Gid9) are ubiquitously expressed and assemble into a high-molecular-weight complex localizing to the nucleus and cytoplasm (Kobayashi *et al*, 2007). The human GID complex (hGID) is also referred to as C-terminal to LisH (CTLH) complex due to a sequence motif shared between five subunits (Kobayashi *et al*, 2007). Like in yeast, the two RING domain-containing subunits RMND5a and MAEA linked by TWA1 form the catalytic core of the E3 ligase (Lampert *et al*, 2018). This catalytic trimer assembles with other subunits, such as WDR26 (Gid7), RanBP9/RanBP10 (Gid1), MKLN1, GID4, ARMC8, and YPEL5 (Kobayashi *et al*, 2007; Lampert

¹ Institute of Biochemistry, Department of Biology, ETH Zürich, Zürich, Switzerland

² Life Science Zürich, PhD Program for Molecular Life Sciences, Zürich, Switzerland

³ Cryo-EM Knowledge Hub (CEMK), Zürich, Switzerland

⁴ Institute of Molecular Systems Biology, Department of Biology, ETH Zürich, Zürich, Switzerland

*Corresponding author. Tel: +41 44 633 65 86; E-mail: matthias.peter@bc.biol.ethz.ch

[†]These authors contributed equally to this work

et al, 2018). Specifically, WDR26 contains a WD40 domain, with a characteristic beta-propeller structure. Such WD40 domains frequently exist in substrate receptors of the Cullin 4 RING E3 ubiquitin ligase family (CRL4) (Angers *et al*, 2006; Higa *et al*, 2006). RanBP9 and RanBP10 contain a SPRY domain, which is commonly present in TRIM RING E3 ligases (DCruz *et al*, 2013), and ARMC8 contains armadillo-like domains, which also serve as platforms for various protein–protein interactions (Huber *et al*, 1997). Interestingly, mammalian cells express two ARMC8 isoforms, ARMC8 α and ARMC8 β , resulting from alternative splicing of the same gene (Kobayashi *et al*, 2007; Tomaru *et al*, 2010; Maitland *et al*, 2019). Both ARMC8 α and ARMC8 β incorporate into the hGID complex (Kobayashi *et al*, 2007; Maitland *et al*, 2019), but the structural and functional differences between the two remain poorly explored. Therefore, although the different subunits are evolutionary conserved and the catalytic core of hGID resembles the yeast complex, further work is required to understand the assembly and structural organization of this intricate E3 ligase in mammalian cells.

The biological functions of the mammalian GID E3 ligase are only beginning to emerge, and to date, there is no evidence that links hGID ligase function to glucose metabolism. Although the binding pocket in human GID4 is conserved, endogenous substrates governed by the Pro/N-end degron motif have not been identified. Of note, the GID complex has been linked to cell proliferation in human cells, at least in part by targeting the transcriptional repressor HMG box protein 1 (HBP1) for proteasomal degradation (Lampert *et al*, 2018). HBP1 inhibits cell cycle progression by regulating the retinoblastoma tumor suppressor (Rb) and it also regulates the expression of genes involved in differentiation and apoptosis. Interestingly, this role of the hGID complex in regulating cell cycle progression and HBP1 stabilization requires not only the catalytic core subunits, but also WDR26/Gid7.

Consistent with this role in cell proliferation, numerous studies have reported significantly increased expression of multiple hGID subunits across a variety of human tumor cells and tissues (Jiang *et al*, 2015a, 2015b, 2016; Both *et al*, 2016; Liang *et al*, 2016; Zhao *et al*, 2016; Zhou *et al*, 2016). Most notably, elevated WDR26 protein levels correlate with poor disease prognosis in many cancers, where available large cancer datasets highlight gene amplification of WDR26 with a remarkable prevalence of up to 55% in breast, ovarian, and prostate cancers (Cerami *et al*, 2012; Gao *et al*, 2013). Additionally, ARMC8 α , but not ARMC8 β , was found to promote cell proliferation and invasion of non-small-cell lung cancer cells (Xie *et al*, 2014). ARMC8 α was also shown to bind and target α -catenin for proteasomal degradation and may interact with hepatocyte growth factor-regulated tyrosine kinase substrate (HRS). However, little is known about the ARMC8 β subunit and its role in the function and regulation of the hGID E3 ligase complex.

Several subunits of the hGID complex, namely RanBP9, RanBP10, WDR26, and MKLN1, have been linked to neurodegeneration and amyloid β (β) pathologies (Woo *et al*, 2015; Her *et al*, 2017), intellectual disability (Skraban *et al*, 2017), and early-onset bipolar diseases and schizophrenia (Bae *et al*, 2015; Nassan *et al*, 2017). Moreover, suppression of RMND5a in *Xenopus laevis* leads to malformations in the fore and midbrain (Pfirrmann *et al*, 2015), suggesting that the GID complex may regulate brain development and neuronal functions. RanBP9 is ubiquitously expressed, and the majority of RanBP9 knock-out mice die immediately after birth

(Puverel *et al*, 2011). The few survivors are significantly smaller in size and cannot undergo spermatogenesis or oogenesis, suggesting that the GID complex may function in growth control and meiosis.

Despite the multitude of evidence supporting a role of the hGID complex in many biological processes, few critical substrates have been identified that can explain the underlying phenotypes. Moreover, it remains unclear whether these diverse cellular functions of the complex require its E3 ligase activity, and if they involve all or just a subset of the known hGID subunits. Therefore, it is crucial to better understand the function and regulation of the different hGID subunits and, in particular, elucidate the mechanism of substrate recruitment.

Previous AP-MS studies not only identified novel hGID subunits, but also sub-stoichiometrically associated proteins such as HBP1, ZMYND19, and HTRA2 (Boldt *et al*, 2016; Lampert *et al*, 2018). HBP1 binds the hGID complex preferentially in proteasome-inhibited cells, consistent with HBP1 serving as a hGID physiological substrate (Lampert *et al*, 2018). HTRA2 encodes a mitochondrial serine protease that induces cell death by regulating cytosolic inhibitors of apoptosis (IAPs), leading to increased caspase activity. Zinc finger MYND domain-containing protein 19 (ZMYND19) interacts with multiple hGID subunits, including TWA1, ARMC8, and RMND5a (Boldt *et al*, 2016). Although ZMYND19 protein levels are upregulated in hepatocellular carcinoma (Zhu *et al*, 2018), its biological function remains unclear.

In this study, we combined cell biology, biochemistry, and cryo-electron microscopy (cryo-EM) to elucidate the assembly and molecular mechanisms of the hGID E3 ligase, with a particular emphasis on subunits involved in substrate recruitment. Interestingly, we found that the hGID E3 ligase engages two independent modules for substrate recruitment, comprised of either WDR26/RanBP9 or GID4/ARMC8. We identified and characterized the minimal hGID complex required for HBP1 degradation *in vitro*, composed of WDR26 together with the catalytic core subunits MAEA, RMND5a, and TWA1. We further showed that ZMYND19 is targeted for degradation by hGID in a GID4-dependent manner, although ZMYND19 lacks a Pro/N-end degron motif. Finally, we propose distinct roles for the ARMC8 isoforms: while both ARMC8 α and ARMC8 β assemble stable hGID complexes, only ARMC8 α is able to recruit GID4.

Results and Discussion

The hGID complex uses distinct substrate modules to target different substrates

In order to identify subunits within the hGID complex that are involved in substrate recruitment, we generated siRNA against ARMC8, GID4, RanBP9, and WDR26. While siRNA-depletion of ARMC8 and GID4 expression did not affect endogenous protein levels of HBP1, reduction of RanBP9 and WDR26 leads to an accumulation of HBP1 in HeLa Kyoto cells (Fig 1A). Likewise, ectopic co-expression of WDR26 and HBP1 prominently decreased HBP1 levels in a MG132-dependent manner, which was not the case when HBP1 was co-expressed with GID4 (Fig 1B). Conversely, over-expression of GID4, but not WDR26, substantially decreased ZMYND19 levels (Fig 1C). Taken together, these data suggest that

HBP1 is targeted for proteasomal degradation in a WDR26/RanBP9-dependent manner, while ZMYND19 is a GID4/ARMC8-dependent substrate of the hGID complex (Fig 1D).

To biochemically test this hypothesis, we conducted *in vitro* ubiquitination assays for HBP1 and ZMYND19 in the presence of hGID complexes with defined subunit composition. Different hGID sub-complexes and full-length GID4 were purified from *Sf9* insect cells using a multi-step column purification (Figs 2A and EV1A–D),

and likewise, the substrates HBP1 and ZMYND19 were expressed and purified to homogeneity (Figs 2B and, EV1E and F). Interestingly, the hGID complex required to achieve efficient HBP1 ubiquitination was composed of the catalytic core (MAEA, RMND5a, and TWA1) together with WDR26 and RanBP9 (Fig 2C). RanBP9 forms a stable complex with WDR26 (Fig EV1G), and the addition of RanBP9 enhanced HBP1 ubiquitination (Fig 2C). The hGID core complex with TWA1, MAEA, and RMND5a does not efficiently

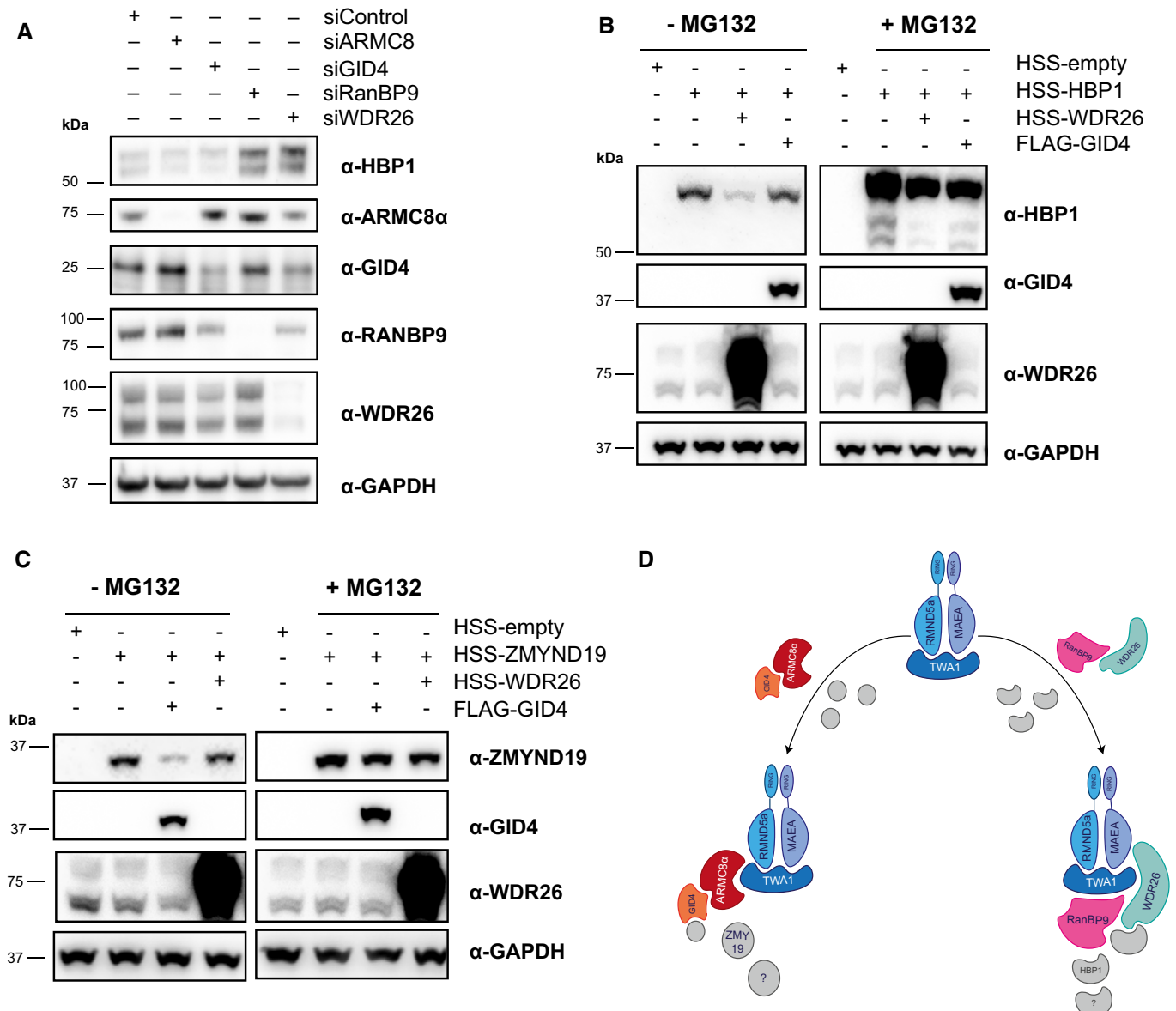


Figure 1. The hGID complex uses distinct substrate modules to target different substrates.

A Immunoblot of cell extracts following depletion of WDR26, RanBP9, ARMC8, and GID4 using pools of siRNAs for 72 h in HeLa Kyoto cells. Endogenous levels of the indicated proteins were monitored by Western blotting ($n = 3$).

B, C Western blotting of samples after ectopic overexpression of HBP1 (B) or ZMYND19 (C) alone, or together with WDR26 or GID4 in HEK-293T cells. HBP1 and ZMYND19 levels were monitored after treatment of MG132 or DMSO for 10–12 h ($n = 3$).

D Schematic representation visualizing the hGID E3 ligase complex using two distinct modules for substrate recruitment.

Source data are available online for this figure.

ubiquitinate HBP1 (Fig EV1H), and the hGID complex lacking both WDR26 and RanBP9, but containing ARMC8, was unable to ubiquitinate HBP1 (Fig 2C). Likewise, hGID complexes composed of the core subunits MAEA, RMND5a, and TWA1, together with ARMC8 and GID4 only poorly ubiquitinated HBP1 *in vitro* (Fig 2D). Addition of GID4 and/or ARMC8 to complexes containing WDR26/RanBP9 had no effect (Fig 2D). Thus, we conclude that WDR26/RanBP9, but not the GID4/ARMC8 module, promotes the E3 ligase activity of the hGID complex toward HBP1.

Conversely, ZMYND19 ubiquitination *in vitro* was dependent on the GID4 subunit. Previous cryo-EM structural analysis of the yeast Gid4-containing GID complex (Gid1, Gid2, Gid4, Gid5, Gid8, and Gid9) reported that Gid4 binds predominantly to Gid5, the yeast ARMC8 homologue (Qiao *et al*, 2019). Likewise, human GID4 also requires ARMC8 full-length (ARMC8 α) to be recruited into the GID complex *in vitro* (Fig EV3A). Yet, a hGID complex containing the core subunits (MAEA, RMND5a, and TWA1) along with WDR26, RanBP9, and ARMC8 was not capable of ubiquitinating ZMYND19, and the ubiquitination activity was only observed in the presence of GID4 (Fig 2E). This ubiquitination was substantially inhibited in the presence of a 10-fold excess of a GID4-specific peptide (Dong *et al*, 2018), consistent with a role of GID4-mediated targeting of ZMYND19. Surprisingly, ZMYND19 does not contain a Pro/N-end degron (Fig 2F), implying that the GID4-binding pocket may also recognize substrates via internal degron motifs.

Together, these results identify ARMC8 α -GID4 and RanBP9-WDR26 as distinct substrate recruitment modules and thus provide a molecular framework for how the human GID E3 ligase recruits its substrates. Other multi-subunit E3 ligase complexes similarly use dedicated subunits for catalytic activity and substrate recruitment. For example, Cullin-RING ligases (CRL) engage one out of a large family of substrate receptors, and their assembly is regulated by substrate availability and the exchange factor CAND1 (Pierce *et al*, 2013). In addition to Gid4, yeast cells express two alternative substrate receptors, Gid10 and Gid11, which all interact with the GID E3 ligase complex through Gid5/ARMC8 (Melnikov *et al*, 2019; Kong *et al*, 2021). Gid4 and Gid10 bind substrates containing nonproline degron motif (Dong *et al*, 2020), and further systematic screening identified many candidates that do not fulfill the Pro/N-end degron criteria (Kong *et al*, 2021). Similarly, human GID4 may also recognize substrates such as ZMYND19 that lack Pro/N-end degron motifs. Nevertheless, GID4-dependent ubiquitination of ZMYND19 *in vitro* required a functional Pro/N-binding pocket, and it will thus be interesting to determine how this substrate class is recognized. Using bioinformatic criteria, no additional mammalian GID4-like substrate receptors have been detected, and it may thus be worth screening for ARMC8 α -interacting proteins to expand the hGID substrate receptor family.

We previously found that WDR26/Gid7 regulates cell cycle progression by targeting the tumor suppressor HBP1 (Lampert *et al*, 2018). Indeed, WDR26 is overexpressed in many human tumors, and, intriguingly, our results suggest that overexpression is sufficient to trigger HBP1 degradation. The cell cycle function of WDR26 requires RanBP9 and the catalytic core subunits, but not ARMC8 α or GID4. Similarly, yeast Gid7 is not necessary to degrade Pro/N-substrates (Qiao *et al*, 2019), and thus, further work is needed to identify cognate WDR26/Gid7 targets.

WDR26/RanBP9-containing hGID complexes assemble ring-shaped tetramers

Size-exclusion purification of the HBP1-targeting hGID complex (MAEA, RMND5a, TWA1, WDR26, and RanBP9) by Superose 6 column showed one predominant peak with an elution profile much larger than the expected monomeric size of 260 kDa. Consistently, oligomerization of hGID was confirmed by SEC-MALS analysis, where the 5-subunit hGID complex (RanBP9, WDR26, MAEA, RMND5a, and TWA1) eluted in a broad peak largely at 1.1 MDa, indicative of a tetrameric assembly (expected molecular weight for a tetramer is 1.06 MDa; Fig 3A). In contrast, hGID complexes lacking RanBP9 (WDR26, MAEA, RMND5a, and TWA1, or ARMC8, MAEA, RMND5a, and TWA1) revealed two peaks with identical subunit composition (Fig EV1C and D), suggesting that RanBP9 is important for complex stability. Oligomerization of the hGID complex also occurs *in vivo*, as shown by co-immunoprecipitation of differentially tagged subunits (Kobayashi *et al*, 2007). Moreover, MAEA, RMND5a, TWA1, WDR26, and RanBP9 are found in the same peak fraction with a proposed molecular weight of more than 1.6 MDa in the SECexplorer web platform (Fig EV1I) (Heusel *et al*, 2019).

To gain better molecular insight into the assembly and oligomerization of the hGID-RanBP9/WDR26 complex, we performed cross-linking mass spectrometry analysis (XL-MS) (Fig 3B). As expected, extended interactions were detected between the two RING domain-containing subunits (MAEA and RMND5a) via their LisH and CTLH domains, which form thermodynamically stable dimers (Gerlitz *et al*, 2005). A dense cross-linking pattern was also detected between RanBP9's LisH and CTLH domains and the CRA domain of TWA1. RanBP9's SPRY domain also interacts with the WD40 domain of WDR26, while no cross-links could be observed between WDR26 and the other subunits (Fig 3B). Based on these data, we speculate that RanBP9 adopts an elongated structure characteristic of a scaffolding function.

To corroborate these interactions, we pursued single particle cryo-electron microscopy (cryo-EM) analysis of the stable hGID complex composed of its catalytic core (MAEA, RMND5a, TWA1) bound to the WDR26/RanBP9 substrate module (Fig EV2A). Single particle analysis of the 5-subunit GID complex (Table EV1) revealed that hGID assembles into a ring-shaped complex with a diameter of ~270 Å. 2D classification of the particles showed circular class averages with twofold symmetry (Scheres, 2016) (Fig EV2B). The circular scaffold is approximately 25 Å wide and is decorated with inward facing protrusions. Comparing the 2D classes revealed that the ring diameter varies slightly, which indicates flexibility of the scaffold ring. Initial model generation with CryoSPARC (Punjani *et al*, 2017) suggested a pseudo-D2 symmetric arrangement, consistent with a tetrameric assembly of the 5-subunit GID complex. To address the conformational flexibility of the scaffold ring, we employed 3D classification after symmetry expansion to refine a cryo-EM map of the tetrameric building block (RanBP9, WDR26, TWA1, MAEA, or RMND5a) to higher resolution (9 Å, FSC = 0.143 criterion; Fig 3C). In the cryo-EM map of the tetrameric building block, we could locate the WD40 propeller of WDR26, which represents the largest protein fold present in the hGID subunits. The resolution did not allow an unambiguous assignment of the alpha-helical modules or other domains. The WD40 propeller of WDR26 protrudes from an elongated scaffold-like density. In the tetramer,

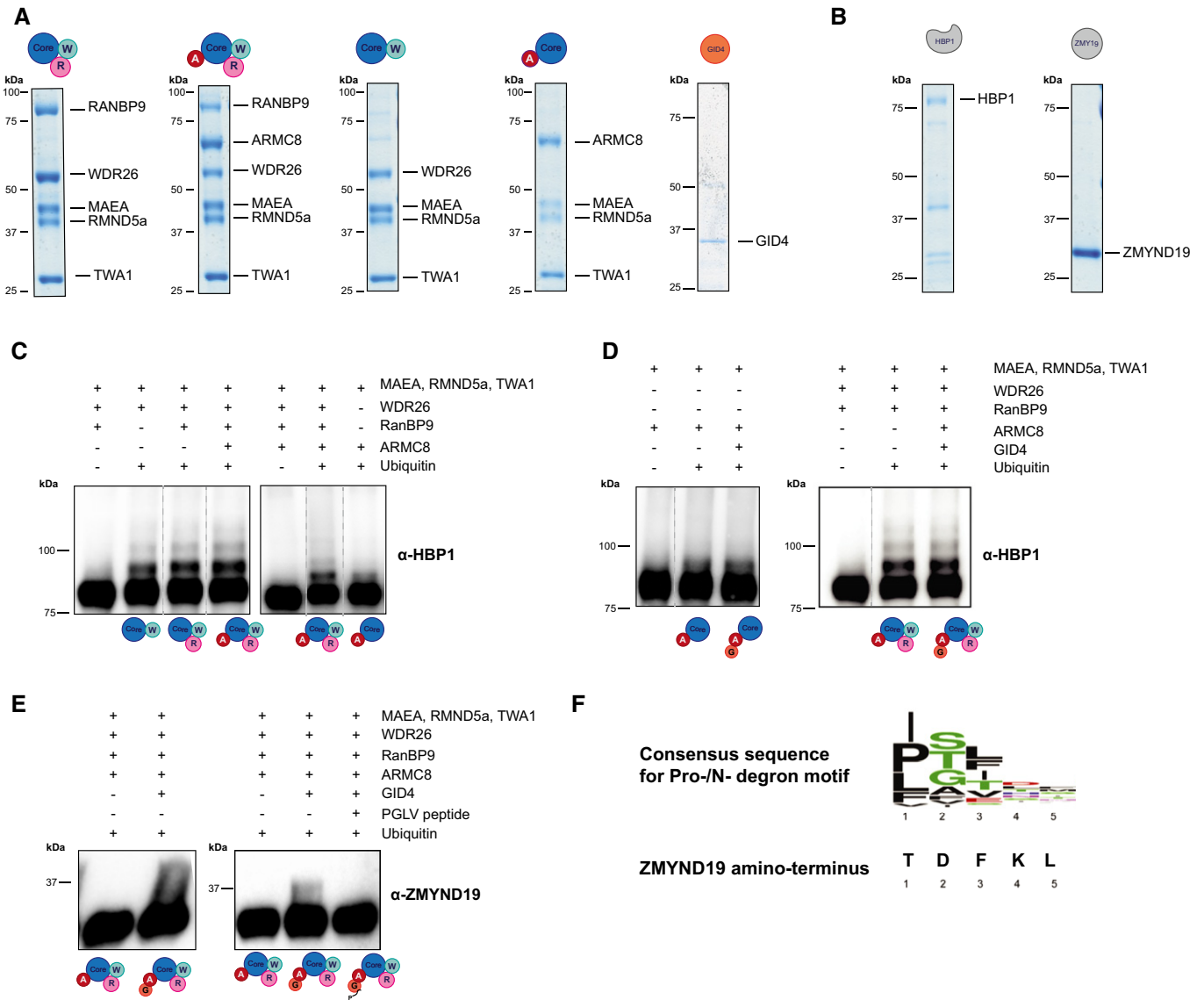


Figure 2. Distinct substrate recruitment modules are required to ubiquitinate HBP1 and ZMYND19 *in vitro*.

- A** Coomassie-stained SDS-PAGE showing purified hGID sub-complexes used for *in vitro* ubiquitination assays. In the schematic representation, the catalytic core composed of MAEA, RMND5a and TWA1 are colored in blue, WDR26 in dark cyan, RanBP9 in light magenta, ARMC8 in dark red, and GID4 in orange.
- B** Coomassie-stained SDS-PAGE showing the purified hGID substrates, HBP1 and ZMYND19.
- C, D** Western blot analysis of *in vitro* ubiquitinated HBP1, which was performed by mixing purified HBP1 with ubiquitin E1, UBCH5a/c, and ubiquitin in the presence of the indicated hGID sub-complexes ($n = 3$).
- E** Immunoblots of *in vitro* ubiquitinated ZMYND19, which was performed by mixing purified ZMYND19 with ubiquitin E1, UBE2H, ubiquitin, and the 6-subunit hGID complex (ARMC8, RanBP9, WDR26, MAEA, RMND5a, and TWA1) in the presence or absence of GID4 and a 10-fold excess of the PGLV GID4-specific peptide ($n = 2$).
- F** Comparison of the N-terminal sequences of the first five amino acids of the Pro/N-end degron consensus motif (Dong *et al*, 2020) and human ZMYND19 (Q96E35).
- Source data are available online for this figure.

two WDR26 subunits contact each other via their WD40 propellers, suggesting a possible role in oligomerization. Moreover, the WD40 propeller seems to be in a conformation primed for substrate recruitment (Fig 3C). To investigate the functional relevance of the WD40 propeller, we overexpressed a WDR26-mutant lacking its WD40 domain, together with HBP1 in HEK-293T cells. Interestingly, this mutant was unable to degrade HBP1 *in vivo* (Fig 3D). Moreover, this interaction was further studied by *in vitro* ubiquitination, and

indeed, this mutant shows a significantly reduced catalytic activity toward HBP1 (Fig 3E), suggesting that the WD40 domain of WDR26 is functionally important. Indeed, the yeast GID complex was shown to be monomeric in the absence of Gid7 (the yeast homologue of WDR26), and addition of Gid7 leads to its oligomeric assembly (Qiao *et al*, 2019; Sherpa *et al*, 2021). Taken together, these data demonstrate that the HBP1-degrading hGID complex composed of MAEA, RMND5a, TWA1, WDR26, and RanBP9 forms a ring-like,

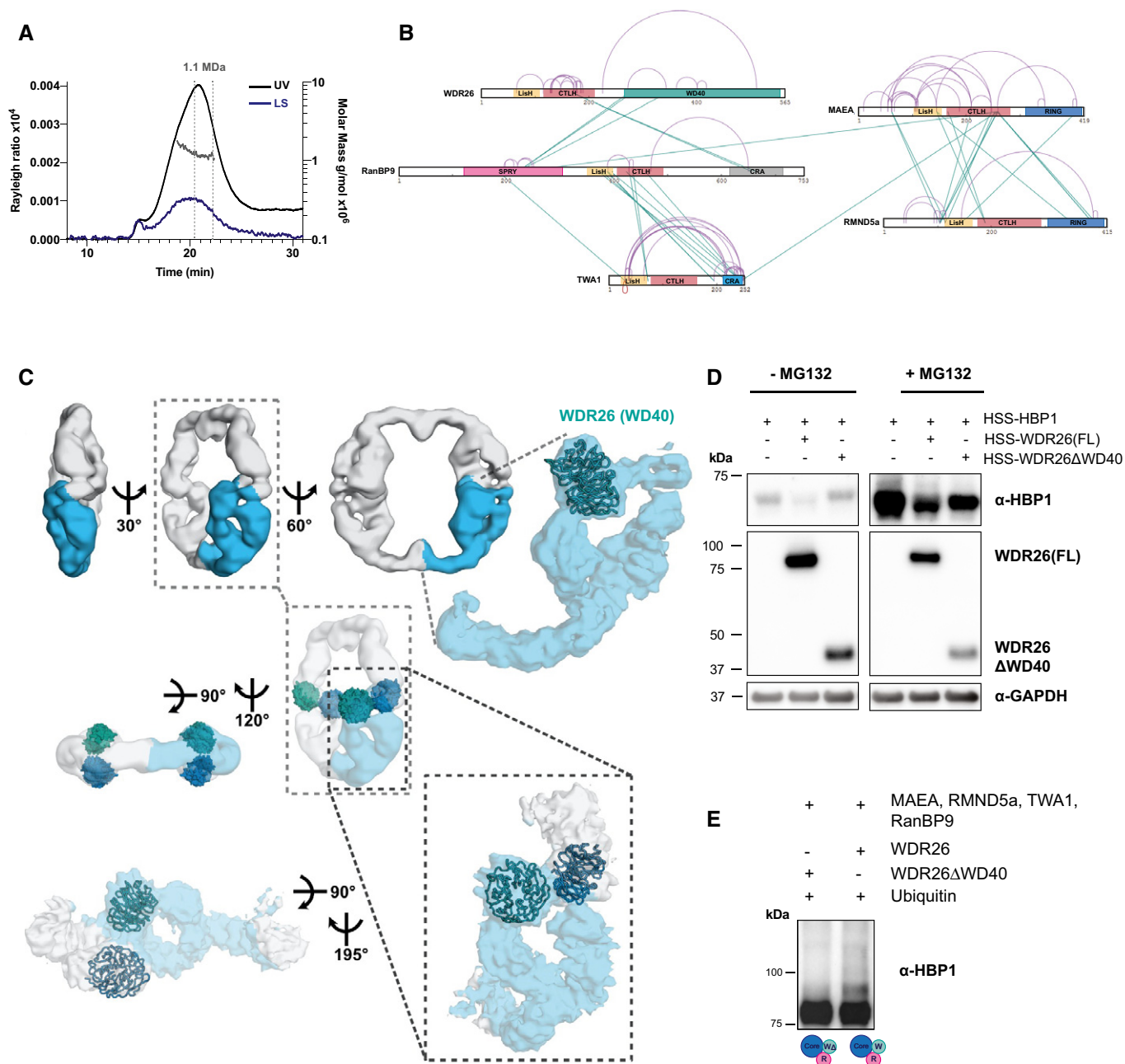


Figure 3. WDR26/RanBP9-containing hGID complexes assemble ring-shaped tetramers.

A Chromatogram of the SEC-MALS analysis at a flow rate of 0.5 ml/min, showing the UV curve and the Rayleigh ratio (1/cm) at a scattering angle of 90 degrees (left y-axis), together with the molar mass (MDa) of the peaks determined by MALS (right y-axis). The peak fraction with a homogenous size distribution at around 1.1 MDa is labeled with gray dotted lines.

B XL-MS analysis of the 5-subunit hGID complex (RanBP9, WDR26, RMND5a, MAEA, and TWA1). Cross-links within different complex subunits are indicated by green lines and cross-links within the same subunit with purple lines. The predicted domain boundaries of the different subunits are colored as follows: LiSH domain in light orange, CTLH domain in dark orange, RING domains in blue, TWA1's CRA domain in light blue, RanBP9's CRA domain in light gray, WD40 in dark cyan, and SPRY in light magenta.

C Rotational views of the cryo-EM map of the 5-subunit hGID complex (RanBP9, WDR26, RMND5a, MAEA, and TWA1) at 11.2 Å resolution. The higher resolution cryo-EM map at 9 Å produced by particle symmetry expansion is shown in blue. The dotted rectangle highlights the positions of the fitted WD40 domains from two tetrameric building blocks.

D Western blotting of samples following ectopic overexpression of HBP1 either alone, or with full-length (FL) or WD40-truncated WDR26 (ΔWD40) in HEK-293T cells. HBP1 levels were monitored in cells treated with MG132 or DMSO for 12–14 h ($n = 3$).

E Western blot analysis of *in vitro* ubiquitinated HBP1 in the presence of wild-type WDR26 (WT) or the WDR26 (ΔWD40) mutant ($n = 2$).

Source data are available online for this figure.

tetrameric structure, possibly stabilized by interactions with the WD40 domains of WDR26.

Fitting the available yeast GID structure (Qiao *et al*, 2019) into the hGID cryo-EM map confirms that the overall structural fold of the GID complex is conserved between yeast and human. Biochemical data demonstrate that the hGID E3 ligase complex uses ARMC8-GID4 as a substrate recognition module, with no direct binding of either ARMC8 or RanBP9 with the catalytic RING domain-containing subunits, suggesting that the central scaffold TWA1 may bridge these interactions. However, while the described yeast GID complex lacks WDR26/Gid7, we found that the human counterpart directly interacts with RanBP9. Thus, consistent with the *in vivo* data, ARMC8 and RanBP9 may function as adaptors to recruit distinct substrate receptors, WDR26 or GID4, respectively. Unlike CRL complexes, the spatial organization of the hGID complex suggests that both WDR26 and GID4 can be recruited at the same time, as they interact through distinct surfaces. The hGID complex may therefore function either as a single unit with separate substrate recruitment modules or as individual complexes that favor one substrate recruitment module over the other.

Interestingly, while the yeast GID complex lacking WDR26/Gid7 is monomeric, the human GID complex assembles into a stable tetramer, with WDR26 and the catalytic RING modules forming oligomerization interfaces at both ends. While this manuscript was under review, a structure of the human GID/CTLH complex was published (Sherpa *et al*, 2021). Consistent with our cryo-EM model, the structure presented by Sherpa and colleagues also shows tetramers of four building blocks composed of RanBP9, WDR26, TWA1, and MAEA or RMND5, which form a ring-shaped assembly through the RING domains of MAEA and RMND5 and two WDR26 subunits. Since hGID tetramers are active, it is possible that the bundled catalytic subunits cooperate with each other to increase poly-ubiquitination of cognate substrates. Alternatively, tetramerization may stabilize hGID complexes, thus favorably position bound substrates and the catalytic core subunits to allow for efficient ubiquitin transfer from the E2 enzymes. However, the relative assembly and arrangement of the distinct substrate-recruiting modules in the tetramer remains to be explored. Finally, analogous to other multimeric complexes, sequestration of subunits may increase their half-life by protecting against autoubiquitination and self-destruction, presumably by burying ubiquitination sites and disordered regions required for proteasomal recognition (Mallik & Kundu, 2018).

Although the functional importance of hGID oligomerization remains unclear, it is interesting to note that similar properties have recently been described for other multi-subunit E3 ligases. For example, DCAF1 promotes oligomerization of CRL4 (Mohamed *et al*, 2021), and the Cul3-BTB adaptor SPOP polymerizes these CRL complexes and drives phase separation in cells (Cuneo & Mittag, 2019). Some E3 ligases are inhibited by oligomerization, while others oligomerize to increase catalytic activity (Balaji & Hoppe, 2020). Thus, further work will be required to understand the mechanism and function of oligomerization of hGID complexes.

ARMC8 α , but not ARMC8 β , recruits GID4 to the core complex, but does not prevent binding of the WDR26/RanBP9 module

Mammalian cells express two main ARMC8 isoforms, ARMC8 α (residues 1–673) and ARMC8 β (residues 1–385; Fig 4A), which are

both expressed at comparable levels in HEK-293T cells (Fig 4B). Interestingly, ARMC8 β lacks the conserved C-terminal domain, which in yeast Gid5 has been implicated in Gid4 binding (Qiao *et al*, 2019) (Fig EV3B). This suggests that ARMC8 α , but not ARMC8 β , is able to recruit GID4. To test this hypothesis, we performed immunoprecipitation assays in HEK-293T cells transiently expressing HSS-ARMC8 α or ARMC8 β along with FLAG-tagged GID4. Indeed, GID4 readily co-purified with ARMC8 α complexes, while ARMC8 β failed to interact with human GID4 *in vivo* (Fig 4C). In contrast, ARMC8 α and ARMC8 β endogenous isoforms co-immunoprecipitated with HSS-tagged WDR26, suggesting that their binding does not compete with the WDR26/RanBP9 module (Fig 4C).

To directly test assembly of these ARMC8 isoforms with GID4 and other members of the GID core complex *in vitro*, we reconstituted hGID complexes containing either ARMC8 α or ARMC8 β (Fig 4D). Importantly, while both ARMC8 α and ARMC8 β readily integrate into the complex, GID4 was only present in ARMC8 α -containing complexes (Fig 4D, lanes 1 and 3). His tag pull-down confirms that GID4 was equally expressed in ARMC8 α and ARMC8 β samples (Fig 4D, lanes 2 and 4). Consistent with this observation, ARMC8 β -containing hGID complexes showed a prominent reduction in GID4-dependent ubiquitination activity compared to ARMC8 α controls (Fig 4E), while the ubiquitination of HBP1 was similar in hGID complexes containing either of the ARMC8 isoforms (Fig 4F). Finally, purified ARMC8 α , but not ARMC8 β , was able to bind GID4 *in vitro* (Fig EV3C). Taken together, these results suggest an isoform-dependent regulation of hGID activity, where ARMC8 β -bound hGID is not able to bind the GID4 substrate receptor and therefore exhibits reduced ubiquitination activity toward GID4 substrates (Fig 4G).

To gain additional molecular insights into the ARMC8 β -containing hGID complex, we analyzed the 6-subunit hGID assembly (MAEA, RMND5a, TWA1, WDR26, RanBP9, and ARMC8 β) by XL-MS and single particle cryo-EM. Size-exclusion purification of this complex by Superose 6 column showed one main peak, indicative of a stable complex of similar size as compared to the 5-subunit complex lacking ARMC8 β (Fig EV3D). ARMC8 β showed prominent cross-links with the C-terminal CRA domain of TWA1 and RanBP9's LisH and CTLH domains (Fig 4H). ARMC8 β also connects to MAEA and RMND5a by several cross-links and forms a dense network of cross-links within the core subunits and RanBP9, suggesting that it closely binds and stabilizes these subunits. Oligomerization was further supported by cross-links between the same lysine residues within MAEA, ARMC8 β , and TWA1 (Fig 4H). Indeed, cryo-EM demonstrated that ARMC8 β -containing hGID complexes maintain the tetrameric ring-like architecture of the 5-subunit hGID complex (Figs 4I and EV3E). However, ARMC8 β -containing hGID complexes appeared more rigid with an extra density near the interface of the subunits, suggesting that ARMC8 β stabilizes the oligomeric assembly (Figs 4J and EV3F).

Identifying the position of ARMC8 β in the hGID assembly (Figs 4I and 5A), and fitting a hGID homology model based on the yeast structure, facilitated the assignment of the remaining GID subunits and domains, such as RanBP9 and TWA1, in the cryo-EM map of the complex (Fig 5B). We generated homology models for ARMC8 β , RanBP9 (SPRY and LisH domain), and TWA1 (LisH, CTLH, and CRA domains) based on the structure of Gid1 and homology modeling of Gid8, respectively (Fig 5B). Consistent with the XL-MS data (Figs 3B and 4H), RanBP9 and TWA1 mediate major

interactions via the LisH and CTLH/CRA domains, respectively (Fig 5B). Furthermore, the SPRY domain of RanBP9 approaches the WD40 domain of WDR26, as also confirmed by several cross-links between these domains (Figs 3B and EV4A). Using *in vitro* pull-down assays, we could also detect direct interaction between TWA1 and WDR26 (Fig EV4B). However, in our fitted model, the WD40 domain of WDR26 is positioned far from ARMC8 β and the RING module, suggesting that WDR26 WD40 domain does not contact these subunits. Based on the yeast GID structure, MAEA (homologue of Gid9) localizes next to TWA1 (Fig 5B and C), which places the catalytic RING module (MAEA or RMND5a) at the second

dimerization interface. *In vitro* pull-down assays did not show direct interaction between the RING module (MAEA and RMND5a) and ARMC8-GID4 nor with RanBP9 (Fig EV4C and D). Rather, TWA1 was necessary to link RanBP9 and ARMC8-GID4 to the catalytic module. Finally, fitting the yeast Gid5-Gid4 module into the cryo-EM map of the human GID complex showed no steric clashes between the two substrate recruitment subunits, GID4 and WDR26 (Fig 5D), which was further confirmed by co-immunoprecipitating WDR26 in GID4 complexes in HEK-293T cells (Fig EV4E). Taken together, these results suggest that hGID complexes may simultaneously engage the two substrate recruitment receptors.

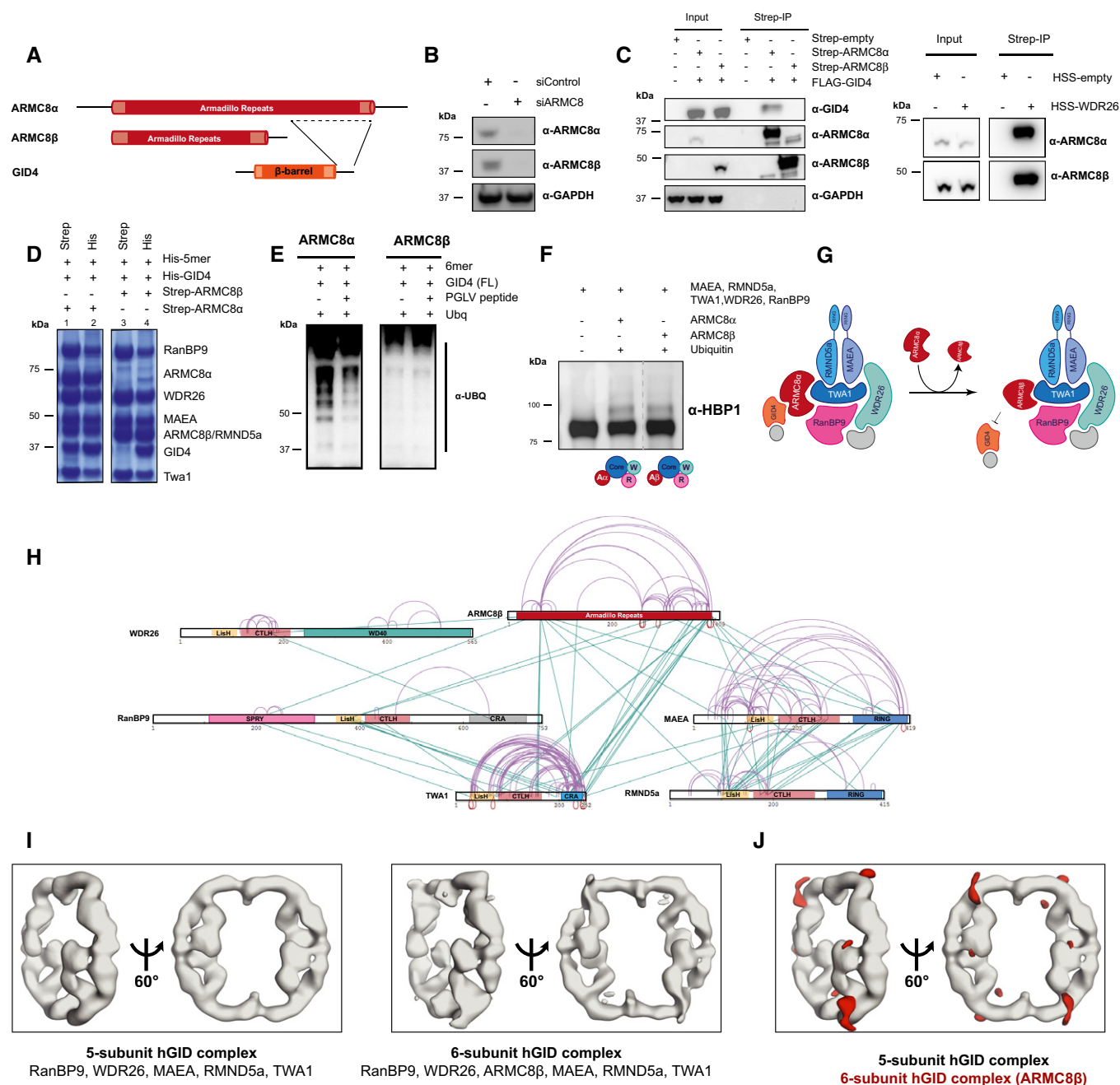
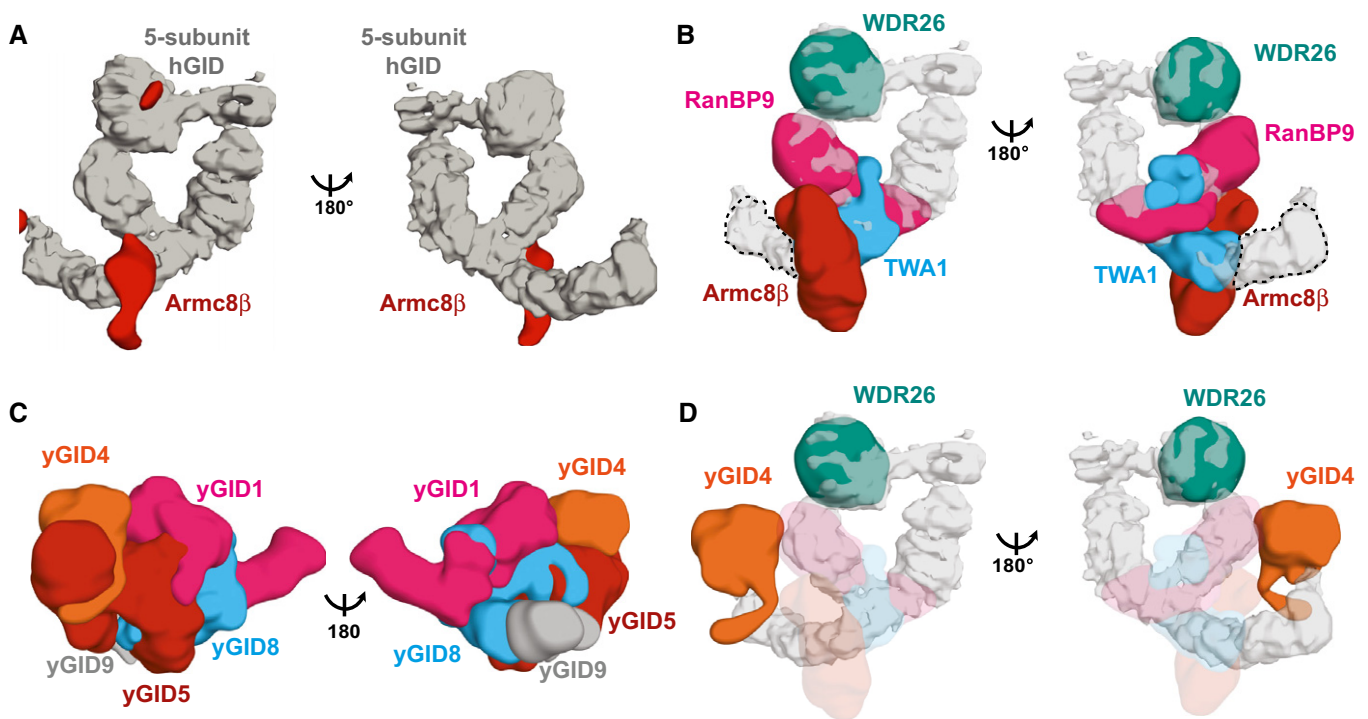


Figure 4.

Figure 4. ARMC8 α but not ARMC8 β recruits GID4 to the core complex in an assembly that does not prevent binding of the WDR26/RanBP9 module.

- A Schematic representation of ARMC8 α (Q8IU7-1), ARMC8 β (Q8IU7-6), and GID4 (Q8IV7-1) proteins. The binding site of GID4 and the C-terminus of ARMC8 α is indicated.
- B Western blot analysis showing the levels of ARMC8 α and ARMC8 β in HeLa Kyoto cells treated for 72 h with control siRNA or siRNA pools against ARMC8 ($n = 3$).
- C Transiently expressed FLAG-GID4 and HSS-tagged ARMC8 isoforms (α or β) in HEK-293T cells. The presence of GID4 in isoform-specific ARMC8 immunoprecipitates was visualized by immunoblotting (left panels). The right panel shows a Western blot of transiently expressed and immunoprecipitated HSS-WDR26 from HEK-293T cells, and the presence of endogenous ARMC8 isoforms (α or β) was probed by immunoblotting ($n = 2$).
- D Baculoviral co-expression in *Sf9* cells of the 5-subunit hGID complex (5mer; His-RanBP9, His-WDR26, FLAG-MAEA, His-RMND5a, and His-TWA1) along with His-GID4 in the presence of Strep-ARMC8 α or Strep-ARMC8 β . Strep- or His-pulldowns revealed the presence of GID4 in ARMC8 α , but not in ARMC8 β , complexes ($n = 3$).
- E Immunoblot analysis of *in vitro* ubiquitinated GID4-hGID complexes containing either ARMC8 α or ARMC8 β (6mer; ARMC8, RanBP9, WDR26, MAEA, RMND5a, and TWA1). Where indicated, the reaction was carried out in the presence of 20-fold molar excess of the PGLV GID4-binding peptide ($n = 3$).
- F Western blot analysis of *in vitro* ubiquitinated HBP1 by the hGID 5-subunit complex in the presence of the different ARMC8 isoforms (α or β ; $n = 2$).
- G Schematic representation illustrating that in contrast to ARMC8 α , incorporation of ARMC8 β prevents hGID activity toward GID4 substrates.
- H XL-MS analysis of the 6-subunit hGID complex (RanBP9, WDR26, RMND5a, MAEA, TWA1, and ARMC8 β). Cross-links within the different complex subunits are indicated by green lines and cross-links within the same subunit by purple lines. The predicted domain boundaries within the different subunits are colored as follows: LisH domain in light orange, CTLH domain in dark orange, RING domains in blue, TWA1's CRA domain in light blue, RanBP9's CRA domain in light gray, WD40 in dark cyan, ARMC8 β in dark red, and the SPRY domain in light magenta.
- I Comparison of the cryo-EM maps of the 5-subunit hGID complex (RanBP9, WDR26, RMND5a, MAEA, and TWA1) and the 6-subunit hGID complex (RanBP9, WDR26, RMND5a, MAEA, TWA1, and ARMC8 β).
- J A difference map (red) shows the extra density in the 6-subunit hGID complex corresponding to ARMC8 β .
- Source data are available online for this figure.

**Figure 5. Comparison and architecture of the human and yeast GID complexes.**

- A ARMC8 β (difference map shown as red surface) binds to the scaffold, distal from the WDR26 WD40 propeller (the 5-subunit hGID map is shown in gray).
- B Homology models of RanBP9 (SPRY and LisH domains; magenta), TWA1 (blue) and the WD40 domain of WDR26 (green) are shown fitted into the map of the 5-subunit hGID complex. A homology model of ARMC8 β fitted into the difference density is shown in red. The approximate position of the RING domain-containing subunit, MAEA or RMND5a, is indicated with a dotted line.
- C The yeast GID complex was superimposed on the cryo-EM map of the 5-subunit hGID complex. The Gid4 (orange), Gid1 (magenta), Gid8 (blue), Gid5 (dark red), and Gid9 (gray) subunits of the yeast structure are shown in the same orientation as the hGID complex.
- D Spatial arrangement of yeast Gid4 with respect to WDR26 is shown in context of the hGID complex.

Several E3 RING ligases regulate their catalytic activity by post-translational modifications, such as phosphorylation, as in the cases of c-Cbl (Levkowitz *et al*, 1999), MDM2 (Khosravi *et al*, 1999), and NEDD4 (Debonneville *et al*, 2001). In addition, CRL activity is activated by covalent attachment of NEDD8, which promotes ubiquitin transfer to bound substrates (Duda *et al*, 2008) and prevents CAND1-mediated exchange of substrate adaptors (Pierce *et al*, 2013), which is critical to dynamically assemble the required repertoire of cellular CRL complexes. Here, we uncovered an unconventional mechanism for how hGID complexes regulate their activity toward ARMC8/GID4 or WDR26/RanBP9-dependent substrates. Indeed, human GID complexes can prevent GID4 recruitment by incorporating the shorter ARMC8 β isoform (Fig 4G), which was previously described as an integral part of the hGID complex (Kobayashi *et al*, 2007; Maitland *et al*, 2019). Our results demonstrate that ARMC8 β incorporation affects neither the oligomeric state (Fig EV3D) nor the overall shape (Fig 4I and J) of the hGID complex, but rather stabilizes its tetrameric structure. Regulating the cellular levels or assembly of ARMC8 α and ARMC8 β into the complex may thus alter the stability of GID4 substrates *in vivo*. It will be interesting to determine whether hGID tetramers have variable ARMC8 α and ARMC8 β ratios and whether cellular factors are needed to exchange these stably bound subunits to differentially modulate hGID-dependent substrate degradation.

Materials and Methods

Cell culture, immunoprecipitation, and Western blot experiments

HeLa Kyoto and HEK-293T were grown in NUNC cell culture dishes in Dulbecco's modified Eagle medium (DMEM, Invitrogen), supplemented with 10% FBS and 1% penicillin–streptomycin–glutamine 100 \times (PSG, Life Technologies). ON-TARGETplus SMARTpool siRNA reagents targeting specific genes (ARMC8 #L-018876-00; hGID4 #L-017343-02; RanBP9 #L-012061-00; WDR26 #L-032006-01; Non-targeting Pool #D-001810-10) were purchased from Horizon Discovery. HeLa Kyoto cells were transfected with 50 nM of siRNA reagents using Lipofectamine 2000 (Thermo Fisher Scientific) according to the manufacturer's specifications. Cells were harvested after 72 h in denaturing urea/SDS buffer, and protein levels of corresponding hGID subunits or HBP1 were detected by immunoblotting.

To co-express HBP1 or ZMYND19 with WDR26, WDR26- Δ WD40, or GID4, 10 cm dishes of HEK-293T cells were transfected with either 6 μ g of pcDNA5-HA-Strep-Strep (HSS)-HBP1 or pcDNA5-HSS-ZMYND19 alone, or together with 6 μ g of pcDNA5-HSS-WDR26, pcDNA5-HSS-WDR26- Δ WD40, or pcDNA5-FLAG-GID4. The media was changed after 6–14 h and treated for 10–12 h with 5 μ M MG132 or DMSO control. Cells were harvested ~48h post-transfection and lysed in 50 mM Tris–HCl pH 8.0, 150 mM NaCl, 1% NP-40, 0.5% sodium deoxycholate, 0.1% SDS, and Complete Protease Inhibitor Cocktail (Roche). Lysates were cleared by centrifugation for 5 min at 2,655 g, and protein concentrations were normalized to 1 mg total protein using buffer containing Tris pH 7.7, 200 mM NaCl, and 0.5 mM Tris(2-carboxyethyl)phosphine (TCEP).

For immunoprecipitation experiments, lysates were loaded on Strep or Flag beads and incubated for 1–2 h at 4°C. Beads were then washed three times with the lysis buffer (40 mM Tris–HCl pH 7.4,

120 mM NaCl, 1 mM EDTA, 0.3% CHAPS, 1 mM PMSF, 10% Glycerol, 0.5 mM TCEP, 1 \times PhosSTOP, and 1 \times Complete Protease Inhibitor Cocktail [Roche]), eluted with SDS-loading dye, and incubated 5 min at 95°C, followed by analysis of bound proteins by immunoblotting.

Proteins were resolved by standard SDS–PAGE or NuPAGE 4–12% Bis–Tris Protein Gels (Invitrogen), followed by transfer onto Immobilon-PVDF or Nitrocellulose membranes (Millipore). Before incubation with the respective primary antibodies, membranes were blocked in 5% milk-PBST (MIGROS) for 1 h. For protein detection primary antibodies against ZMYND19 (ab86555, Abcam), HBP1 (11746-1-AP, Protein Tech Group, and sc-376831, SantaCruz), ARMC8 (sc-365307, SantaCruz), GID4 (kind gift of B. Schulmann, and PA5-69987, Invitrogen), WDR26 (A302-244A, Bethyl Laboratories), TWA1 (5305, Prosci-Inc), MAEA (AF7288-SP, R&D Systems Europe Ltd), RanBP9 (A304-779A, Bethyl Laboratories), FLAG (M2, F3165, Sigma-Aldrich or F7425, Sigma-Aldrich), ubiquitin conjugates (P4D1, sc-8017, Santa Cruz), and GADPH (G-8795, Sigma-Aldrich) were used. Secondary antibodies used included goat anti-mouse IgG HRP (170-6516, Bio-Rad) and goat anti-rabbit IgG HRP (170-6515, Bio-Rad). Proteins were visualized with SuperSignal™ West Chemiluminescent Substrate solution (Thermo Fisher) and scanned on a Fusion FX7 imaging system (Witec AG). For re-probing, blots were stripped in ReBlot Plus stripping buffer (2504, Millipore) and washed several times in PBST.

Sf9 protein expression and purification

cDNAs encoding human ARMC8 α (NP_001350870.1), ARMC8 β (NP_054873.2), RanBP9, TWA1, MAEA, RMND5a, HBP1, GID4, ZMYND19, WDR26 (121–661), and WDR26 (Δ WD40; 121–319) were cloned into pAC8 vector, which is derived from the pBacPAK8 system (ClonTech). Recombinant baculoviruses were prepared in *Spodoptera frugiperda* (Sf9) cells using the Bac-to-Bac system (Life Technologies). Recombinant protein complexes were expressed in Sf9 by co-infection of single baculoviruses. For the 5-subunit hGID complex (RanBP9, MAEA, RMND5a, WDR26, and TWA1), RanBP9 was expressed with N-terminal Strep (II) tag, MAEA with N-terminal FLAG tag, and RMND5a, WDR26, and TWA1 with N-terminal His tag. For the 6-subunit hGID complex (ARMC8, RanBP9, MAEA, RMND5a, WDR26, and TWA1), ARMC8 α or ARMC8 β was expressed with an N-terminal Strep (II) tag, MAEA with N-terminal FLAG tag, RanBP9, and RMND5a, WDR26, and TWA1 with an N-terminal His tag. For the 4-subunit hGID complexes MAEA, RMND5a, WDR26, and TWA1, or MAEA, RMND5a, ARMC8, and TWA1, WDR26 or ARMC8 were expressed with N-terminal Strep (II) tag, MAEA with N-terminal FLAG tag and RMND5a, and TWA1 with N-terminal His tag. Full-length HBP1 was expressed with an N-terminal glutathione S-transferase (GST) tag, and ZMYND19 and GID4 were expressed with an N-terminal Strep (II) tag. Cells were harvested 36–48 h after infection and lysed by sonication in a buffer containing Tris–HCl pH 7.7, 200 mM NaCl, and 0.5 mM TCEP, including 0.1% Triton X-100, 1 \times protease inhibitor cocktail (Roche Applied Science) and 1 mM phenylmethanesulfonyl fluoride (PMSF). Lysates were cleared by ultracentrifugation for 45 min at 40,000 g. The supernatant was loaded on Strep-Tactin (IBA life sciences) affinity chromatography beads in buffer containing Tris–HCl pH 7.5, 200 mM NaCl and 0.5 mM TCEP. The Strep (II) elution

fractions were further purified via ion exchange chromatography (Poros HQ 50 μm , Life Technologies) and subjected to size-exclusion chromatography in a buffer containing 50 mM HEPES pH 7.4, 200 mM NaCl, and 0.5 mM TCEP. For GID4 and HBP1, 10% of glycerol was added to all buffers. GID4 was purified by size-exclusion chromatography in a buffer containing 50 mM MES pH 6.5, 200 mM NaCl, and 0.5 mM TCEP. Pure fractions, as judged by SDS-PAGE, were collected and concentrated using 10,000 MWT cut-off centrifugal devices (Amicon Ultra) and stored at -80°C .

Size-exclusion chromatography-multi-angle light scattering (SEC-MALS)

The oligomeric state of the 5-subunit hGID complex (RanBP9, WDR26, MAEA, RMND5a, and TWA1) was investigated by multiangle light scattering (MALS) coupled with size-exclusion chromatography (SEC). SEC was performed on an Agilent 1200 HPLC system equipped with a diode array detector (DAD) using a Superose 6 10/300 column (Cytiva) in 50 mM HEPES pH 7.4, 200 mM NaCl, and 1 mM TCEP. Data from the DAD and miniDAWN Treos-II (Wyatt Technology) were processed with the Astra V software to determine the weight averaged molar mass of the protein complex in the main eluting peak, where the calculated protein extinction coefficient of 1,000 ml/(g cm) and the average protein dn/dc of 0.185 ml/g were used.

In vitro ubiquitination and pull-down assays

In vitro ubiquitination assays were performed by mixing 0.35 μM hGID complexes and 0.2 μM HBP1 or 0.35 μM ZMYND19 with a reaction mixture containing 0.1 μM E1 (UBA1, BostonBiochem), 1 μM E2 (UBCH5a and UBCH5c, or UBE2H, BostonBiochem), and 20 μM Ubiquitin (Ubiquitin, BostonBiochem). Where indicated, 2 μM GID4 and 20 μM of synthetic GID4-binding peptide (PGLV) were added. Reactions were carried out in 50 mM Tris pH 7.7, 200 mM NaCl, 10 mM MgCl_2 , 0.2 mM CaCl_2 , 3 mM ATP, 2 mM DTT, 0.1 \times Triton X, 10% glycerol, and 0.1 mg/ml BSA and incubated for 120 min at 35°C . The *in vitro* ubiquitination reactions of HBP1 by the core hGID complex (MAEA, RMND5a, and TWA1), or the 5-subunit hGID complex with WDR26 (ΔWD40), were incubated at 35°C for 30 min. *In vitro* ubiquitination of HBP1 by the GID4-hGID complexes was done with 0.25 μM HBP1 and 0.35 μM hGID 6-subunit complex (either with ARMC8 α or ARMC8 β). Reactions were stopped with SDS-loading dye and analyzed by Western blot using anti-HBP1 (11746-1-AP, Protein Tech Group, 1:500) or anti-ZMYND19 antibody (ab86555, Abcam, 1:500).

For GID4-dependent *in vitro* ubiquitination reactions, 0.35 μM hGID complexes (RANBP9, MAEA, RMND5a, WDR26, and TWA1) with either ARMC8 α or ARMC8 β were mixed with 0.2 μM ZMYND19 and 2 μM GID4, in the presence or absence of 40 μM GID4-binding synthetic peptide (PGLV). Reactions were carried out in 50 mM Tris pH 7.7, 200 mM NaCl, 10 mM MgCl_2 , 0.2 mM CaCl_2 , 3 mM ATP, 2 mM DTT, 0.1 \times Triton X, 10% glycerol, and 0.1 mg ml^{-1} BSA and incubated for 120 min at 33°C . Reactions were then analyzed by western blot using anti-Ubiquitin (P4D1) primary antibody (Santa Cruz).

For pull-down assays in *Sf9* cells, 100 μl of baculoviruses of the 5-subunit hGID complex: His-RanBP9, His-WDR26, FLAG-MAEA, His-RMND5a, and His-TWA, with His-GID4 and Strep-ARMC8 α or Strep-Armc8 β were co-infected in 10 ml of *Sf9* cells. Infected cells

were incubated at 27°C for 48 h and lysed by sonication in a buffer containing Tris-HCl pH 7.7, 200 mM NaCl, and 0.5 mM TCEP, including 0.1% Triton X-100, 1 \times protease inhibitor cocktail (Roche Applied Science), and 1 mM PMSF. Lysates were cleared by centrifugation at 14,000 g for 30 min, and 1 ml of soluble protein fractions was incubated for 1 h at 4°C with 20 μl Strep-Tactin Macroprep beads (IBA Lifesciences). Beads were washed three times with lysis buffer, and bound proteins were eluted in 20 μl of SDS-loading dye and heated at 95°C for 2 min.

Cross-linking mass spectrometry

Two different cross-linking protocols were used, based on the amine-reactive disuccinimidyl suberate (DSS) (Leitner *et al*, 2013) and a combination of pimelic dihydrazide (PDH) and the coupling reagent 4-(4,6-dimethoxy-1,3,5-triazin-2-yl)-4-methylmorpholinium (DMTMM) chloride (Leitner *et al*, 2014; Mohammadi *et al*, 2021). DSS was obtained as a 1:1 mixture of “light” (d_0) and “heavy” (d_{12}) isotopic variants from Creative (d_0) PDH from ABCR, heavy (d_{10}) PDH and DMTMM chloride from Sigma-Aldrich.

Cross-linking conditions were optimized in screening experiments on the 5-subunit hGID complex using SDS-PAGE as a read-out, and 1 mM DSS (d_0/d_{12}) and 22 mM PDH (d_0/d_{10}) + 4.4 mM DMTMM were selected as the optimal conditions. The low concentration of DMTMM relative to PDH results in the dominant formation of zero-length cross-links over the integration of the dihydrazide linker (Mohammadi *et al*, 2021). For XL-MS, protein complexes were prepared at a total protein concentration of 1 mg/ml in a buffer containing 50 mM HEPES pH 7.4, 200 mM NaCl, and 1 mM TCEP and cross-linked at 50 μg scale. DSS cross-linking was performed at 37°C for 30 min, followed by a quenching step (50 mM NH_4HCO_3) for 30 min at the same temperature. PDH+DMTMM cross-linking was performed for 45 min at 37°C followed by removal of the reagents by gel filtration (Zeba spin desalting columns, Thermo Fisher Scientific).

After quenching or gel filtration, samples were dried in a vacuum centrifuge and redissolved in 8 M urea solution for reduction (2.5 mM tris-2-carboxyethyl phosphine, 37°C , 30 min) and alkylation (5 mM iodoacetamide, 23°C , 30 min in the dark) steps. Samples were diluted to ~ 5.5 M urea with 150 mM NH_4HCO_3 before addition of endoproteinase Lys-C (Wako, 1:100, 37°C , 2 h), followed by a second dilution step to ~ 1 M urea with 50 mM NH_4HCO_3 and addition of trypsin (Promega, 1:50). After overnight incubation at 37°C , samples were acidified to 2% (v/v) formic acid and purified by solid-phase extraction (SepPak tC18 cartridges, Waters). Purified samples were fractionated by peptide-level size-exclusion chromatography (SEC) (Leitner *et al*, 2012, 2013) using Superdex Peptide PC 3.2/300 (for the 5-subunit hGID complex) or Superdex 30 Increase 3.2/300 (for the 6-subunit hGID complex) columns (both GE Healthcare). Three high-mass fractions enriched in cross-linked peptide pairs were collected for MS analysis.

Liquid chromatography-tandem mass spectrometry (LC-MS/MS) was performed on an Easy nLC 1200 HPLC system connected to an Orbitrap Fusion Lumos Mass Spectrometer (both Thermo Fisher Scientific). Peptides were separated on an Acclaim PepMap RSLC C₁₈ column (250 mm \times 75 μm , Thermo Fisher Scientific). The LC gradient was set from 9 to 40% mobile phase B in 60 min, mobile phases were A = water/acetonitrile/formic acid (98:2:0.15, v/v/v)

and B = acetonitrile/water/formic acid (80:20:0.15, v/v/v), and the flow rate was 300 nl/min.

Each SEC fraction was injected in duplicate with two different data-dependent acquisition methods for MS analysis. Both used a top-speed method with 3 s cycle time and detection of precursors in the Orbitrap analyzer at 120,000 resolution. Precursors were selected whether they had a charge state between 3+ and 7+ and an m/z between 350 and 1,500, and fragmented in the linear ion trap at a normalized collision energy of 35%. The high-resolution method used detection of the fragment ions in the Orbitrap at 30,000 resolution, while the low-resolution method used detection in the linear ion trap at rapid scan speed. The two different methods were selected to benefit from either the higher mass accuracy of the Orbitrap or the higher sensitivity of ion trap detection. xQuest (version 2.1.5, available from https://gitlab.ethz.ch/leitner_lab/xquest_xprophet [Walzthoeni *et al*, 2012; Leitner *et al*, 2013]) was used to identify cross-linked peptide pairs. MS/MS spectra were searched against custom databases containing the target protein sequences and contaminant proteins and their randomized entries. Important search parameters included the following: enzyme specificity = trypsin (no cleavage before P) with maximum two missed cleavages, precursor mass tolerance = 15 ppm, fragment mass tolerance = 15 ppm for Orbitrap detection or 0.2/0.3 Da (common/cross-link ions) for ion trap detection. Oxidation of Met was selected as a variable modification, carbamidomethylation of Cys as a fixed modification. DSS was assumed to react with Lys or the protein N termini; PDH was assumed to react with Asp and Glu; DMTMM was assumed to react with Lys and Asp or Lys and Glu. Primary search results were filtered with a more stringent error tolerance (−5 to +1 ppm for the 5-subunit hGID complex, 0 to +5 ppm for the 6-subunit hGID complex) and required to have xQuest deltaS scores ≤ 0.9 and TIC scores ≥ 0.1 (DSS) or ≥ 0.15 (DMTMM). The remaining spectra were manually evaluated to have at least four bond cleavages in total per peptide or three consecutive bond cleavages per peptide. Ambiguous identifications containing peptides that could be mapped to more than one protein (from tags) were removed. Finally, an xQuest score cut-off was selected so that the false-positive rate was at 5% or less at the non-redundant peptide pair level. All cross-link identifications are provided in Datasets EV1–EV4. The mass spectrometry proteomic data have been deposited to the ProteomeXchange Consortium (<http://proteomecentral.proteomexchange.org>) via the PRIDE partner repository (Perez-Riverol *et al*, 2019) with the dataset identifier PXD024822. XL-MS data in Figs 3B and 4H were visualized with xiNET (Combe *et al*, 2015).

Sample preparation and cryo-electron microscopy analysis

In order to increase the stability of the 5- and 6-subunit hGID complexes, the gradient fixation (GraFix) protocol was applied (Stark, 2010). Briefly, samples were loaded on a glycerol gradient (10–40% w/v) in the presence of the cross-linker glutaraldehyde (0.25% v/v added to the 40% glycerol solution), followed by ultracentrifugation (SW40Ti rotor) at 125,750 g for 18 h at 4°C. Peak fractions containing the protein complexes were collected, and buffer exchange for glycerol removal was performed by Zeba Spin columns in a buffer containing 50 mM HEPES pH 7.4, 200 mM NaCl, 1 mM TCEP and either 0.01% NP-40 for the 5-subunit hGID complex or 0.05% NP-40 for the 6-subunit hGID complex. 4 μ l sample (0.08–0.15 mg/ml) was then applied on glow discharged

Quantifoil holey grids (R2.2, Cu 300 mesh, Quantifoil Micro Tools GmbH, Grossl bichau, Germany) coated with a continuous 1 nm carbon film. Grids were incubated for 20–60 s at 4°C and 100% humidity, blotted for 1 s with Whatman no.1 filter paper, and vitrified by plunging into liquid ethane (Vitrobot, Thermo Fischer).

Data collection

Three datasets of 5-subunit GID and one dataset of GID-ARMC8  complexes were collected with the Titan Krios cryo-electron microscope (Thermo Fisher Scientific Inc., Waltham MA) operated at 300 kV, using the K2 and K3 direct electron detectors (Gatan Inc., Pleasanton CA), operated in counting or super-resolution mode. Data collection parameters are compiled in Table EV1.

Cryo-EM Data analysis of the 5-subunit hGID map

Data acquisition and preprocessing

All micrographs were drift corrected with MotionCor2 using a 5-by-5 patch (Li *et al*, 2013). In addition, micrographs recorded on the K3 detector in super-resolution mode were binned twofold with MotionCor2. Defocus of the drift-corrected averages was determined by CTF fitting with Gctf (Zhang, 2016). For each dataset, particles from 10 micrographs representative of the defocus range of the entire dataset were manually selected. Selected particle positions were used to train a neural network in order to select particles of the entire dataset with crYOLO (Wagner *et al*, 2019). A total of 815,538 particles were selected (88,564 from dataset 1, 538,734 from dataset 2, 188,240 from dataset 3). Accuracy of automated particle selection was verified by manual inspection of particle positions.

2D Classification (5-subunit GID)

Image processing was carried out in Relion 3.1 (Scheres, 2016). Particles from datasets 1, 2, and 3 were extracted (box size 720, scaled to 96 pixels, resulting pixel size 6.3  /pixel) and combined into a single stack with 815,538 particles. Particles were subjected to two rounds of 2D classification into 100 classes. After the first round, 569,845 particles (69%) were selected, rejecting obvious junk classes (ice blobs, edges). The selected particles were subjected to 2D classification in a second round with 429,682 particles selected (75%) after removal of junk classes and obviously broken particles. The selected particles were re-extracted with a box size of 720 pixels, scaled to 180 pixels (resulting pixel size: 3.38  /pixel), and recentered to shifts applied during classification.

Initial model generation

An initial model of 5-subunit GID complex was generated in cryoSPARC (Punjani *et al*, 2017). Particles selected from datasets 2 and 3 of 5-subunit GID complex were extracted with a box size of 640 pixels and binned to 128 pixels (pixel size: 3.36  /pixel). After one round of 2D classification, junk classes (ice blobs, edges) were discarded and the remaining particles were used for initial model generation with three classes. The initial model generation without application of symmetry or with C2 symmetry resulted in ring-shaped reconstruction with a strong density for one-half of the ring and twofold symmetry. The application of D2 symmetry resulted in a ring-shaped reconstruction that matched the map for the initial models calculated with C1 and C2 symmetry and showed projections corresponding to the ring-shaped class averages. This model was used as an initial

model for heterogeneous refinement into three classes resulting in three maps that were very similar, where one of which, at a resolution of 11.2 Å (loose mask, FSC = 0.143 criterion), was chosen as the initial model for further processing.

3D structure refinement

Particles were 3D classified into 10 classes without application of symmetry, using the initial model generated with cryoSPARC. The reconstruction of class 10 showed the hallmark intact ring-shaped 5-subunit GID complex with pseudo-D2 symmetry. Class 10 contained 39,255 particles, which corresponded to ~9.1% of all particles that entered classification. As we aimed at a focused refinement for the WDR26, TWA1, RanBP9 subcomplex, we symmetrized the map with D2 symmetry before particle symmetry expansion. After a first refinement, another step of re-centering and subsequent 2D classification (36,134 particles selected, 92%) was applied and the particles were refined with application of D2 symmetry in preparation for symmetry expansion. The refined particles were D2 symmetry expanded using the `reion_particle_symmetry_expand` function, resulting in 144,536 tetrameric building blocks. One tetrameric building block (encompassing WDR26, TWA1, RanBP9, and MAEA or RMND5a) with additional density at the edges (including the second WDR26 beta-propeller) was carved from the refined map using Chimera volume eraser to create a soft-edged mask. The mask, the map, and the expanded particles were all recentered to the map center of mass. The symmetry expanded, recentered particles were subjected to 3D classification. The class that showed detailed structural features in agreement with the map calculated before symmetry expansion contained 33,929 ASU particles and was subjected to a 3D refinement resulting in a 9 Å resolution map (FSC 0.143 criterion).

Cryo-EM data analysis of the 6-subunit hGID map (The 5-subunit GID and ARMC8 β complex)

In order to localize ARMC8 β in the GID complex, a difference map between the 5-subunit GID and the GID-ARMC8 β complex was calculated. Drift correction of micrographs was performed with MotionCorr (Li *et al*, 2013), and defocus of the drift-corrected averages was determined by CTF fitting with Gctf (Zhang, 2016), resulting in a dataset of 3,048 micrographs. Particles from 10 representative micrographs were manually selected and used to train a neural network in order to pick particles of the remaining dataset with crYOLO (Wagner *et al*, 2019). A total of 73,559 GID-ARMC8 β particles were selected, and accuracy of automated particle selection was verified by manual inspection. A combined set of particles from datasets 2 and 3 of the 5-subunit GID complex was used to calculate a map for comparison, undergoing identical processing steps as the GID-ARMC8 β data. Particles were extracted and binned to the same pixel size of 8.4 Å/pixel (5-subunit GID: 726,955 particles, box size 640 pixels, scaled to box size of 64 pixels, GID-ARMC8 β complex: 73,559 particles, box size 504 pixels, scaled to a box size of 64 pixels). Both sets were subjected to one round of 2D classification into 100 classes where obvious junk classes showing ice contaminations or carbon edges were removed. The 5-subunit GID particle set was reduced to 452,950 particles, GID-ARMC8 β to 44,062 particles. The 5-subunit GID dataset was randomly split, and 44,062 particles were selected. After re-extraction with a box size of 128 pixels and a pixel size of 4.2 Å/pixel, both particle sets were refined with application of C2 symmetry to produce the final

maps (GID: 23 Å resolution, GID-ARMC8 β : 24 Å resolution). Maps were aligned, and difference density was calculated in UCSF Chimera.

Cryo-EM map interpretation

Models for RanBP9 (172–463), TWA1 (27–238), the WD40 domain of WDR26 (349–547), and ARMC8 β (31–407) were obtained using homology modeling in Phyre2 (Mezulis *et al*, 2015) and the crystal structure of the SPRY domain of human RanBP9 (PDB 5JI7, Hong *et al*, 2016). The ring-shaped WD40 domain of WDR26 was fitted into the cryo-EM map with the Chimera (Pettersen *et al*, 2004) fit command (highest correlation 0.95). For the RanBP9, TWA1 and ARMC8 β subunits of the GID complex, a homology model was assembled by superimposing the homology structures on the yeast GID coordinates (PDB 6SWY; Qiao *et al*, 2019). The model was placed in the cryo-EM map based on the elongated shape of the ARMC8 β difference density, and ARMC8 β was rigid body docked into the difference density. Based on the placement of ARMC8 β , TWA1/RanBP9 was separately fitted as a rigid body into the ASU map. Subunit placements were cross-checked with cross-linking MS results. For visualization, surface representations of the domains were filtered to 10 Å. Images were created using PyMOL (PyMOL, version 2.4.0. New York: Schrodinger Inc.).

Data availability

The datasets produced in this study are available in the following databases:

Electron Microscopy databank: Cryo-EM maps are deposited in the EMDB under accession codes EMD-13206 (tetrameric building block of the human GID complex, <https://www.ebi.ac.uk/emdb/entry/EMD-13206>), EMD-13207 (the human GID complex, <https://www.ebi.ac.uk/emdb/entry/EMD-13207>), EMD-13209 (5-subunit human GID complex, <https://www.ebi.ac.uk/emdb/entry/EMD-13209>), and EMD-13210 (6-subunit human GID complex, <https://www.ebi.ac.uk/emdb/entry/EMD-13210>).

Proteomics Identification database: Cross-linking Mass Spectrometry: All cross-link identifications are provided in Datasets EV1–EV4. The mass spectrometry proteomic data have been deposited to the ProteomeXchange Consortium (<http://proteomecentral.proteomexchange.org>) via the PRIDE partner repository (Perez-Riverol *et al*, 2019) with the dataset identifier (PXD024822). <https://www.ebi.ac.uk/pride/archive/projects/PXD024822>.

Expanded View for this article is available online.

Acknowledgements

We would like to thank Jason Greenwald for performing the MALS analysis of the 5-subunit GID complex and Anton Khmelinskii for sharing unpublished results. We are grateful to Anna Maria Stier, Halil Bagci, and members of the Peter lab for helpful discussions, and Alicia Smith for critical editing. We thank Eliane Züger for help with the ARMC8 isoforms, and Mahshid Gazorpak and the ETH block course students for initial overexpression experiments. We thank ScopeM and in particular Miroslav Peterek for microscopy training and support. We acknowledge Ruedi Aebersold and Paola Picotti for access to the Orbitrap Fusion Lumos mass spectrometer, which was funded by the ETH Scientific Equipment program and the European Union Grant ULTRA-DD (FP7-JTI 115766). Sophia Park profits from an ITN network grant from the European

Research Commission (860517). This work was supported by the Swiss National Science Foundation (310030_179283/1), the Swiss Cancer League (KLS-4574-08-2018), a donation from Dr. Walter Fischli and the ETH Zürich. Open access funding provided by Eidgenössische Technische Hochschule Zurich.

Author contributions

WIM and MP conceptualized the study. WIM carried out the biochemical experiments, and WIM and SLP performed the cellular assays. WIM prepared the specimens for EM data collection, JR, DB, and WIM imaged EM grids, and JR, WIM, and DB processed the EM data. AL performed the XL-MS analysis. MP and WIM wrote the manuscript, with critical input from all authors. Open access funding provided by Eidgenössische Technische Hochschule Zürich.

Conflict of interest

The authors declare that they have no conflict of interest.

References

- Angers S, Li T, Yi X, MacCoss MJ, Moon RT, Zheng N (2006) Molecular architecture and assembly of the DDB1-CUL4A ubiquitin ligase machinery. *Nature* 443: 590–593
- Bae JS, Kim JY, Park B-L, Cheong HS, Kim J-H, Namgoong S, Kim J-O, Park CS, Kim B-J, Lee C-S et al (2015) Investigating the potential genetic association between RANBP9 polymorphisms and the risk of schizophrenia. *Mol Med Rep* 11: 2975–2980
- Balaji V, Hoppe T (2020) Regulation of E3 ubiquitin ligases by homotypic and heterotypic assembly. *F1000Res* 9: 1–8
- Boldt K, van Reeuwijk J, Lu Q, Koutroumpas K, Nguyen T-M, Texier Y, van Beersum SEC, Horn N, Willer JR, Mans DA et al (2016) An organelle-specific protein landscape identifies novel diseases and molecular mechanisms. *Nat Commun* 7: 1–13
- Both J, Wu T, ten Asbroek ALMA, Baas F, Hulsebos TJM (2016) Oncogenic properties of candidate oncogenes in chromosome region 17p11.2p12 in human osteosarcoma. *Cytogenet Genome Res* 150: 52–59
- Cerami E, Gao J, Dogrusoz U, Gross BE, Sumer SO, Aksoy BA, Jacobsen A, Byrne CJ, Heuer ML, Larsson E et al (2012) The cBio cancer genomics portal: an open platform for exploring multidimensional cancer genomics data. *Cancer Discov* 2: 401–404
- Chen S-J (2017) An N-end rule pathway that recognizes proline and destroys gluconeogenic enzymes. *Science* 355: 1–9
- Combe CW, Fischer L, Rappsilber J (2015) xiNET: cross-link network maps with residue resolution. *Mol Cell Proteomics* 14: 1137–1147
- Cuneo MJ, Mittag T (2019) The ubiquitin ligase adaptor SPOP in cancer. *FEBS J* 286: 3946–3958
- D’Cruz A, Kershaw N, Chiang J, Wang M, Nicola N, Babon J, Gack M, Nicholson S (2013) Crystal structure of the TRIM25 B30.2 (PRYSPRY) domain: a key component of antiviral signalling. *Biochemistry* 456: 231–240
- Debonneville C, Flores SY, Kamynina E, Plant PJ, Tauxe C, Thomas MA, Münster CM, Chraïbi A, Pratt JH, Horisberger E-D et al (2001) Phosphorylation of Nedd4-2 by Sgk1 regulates epithelial Na⁺ channel cell surface expression. *EMBO J* 20: 7052–7059
- Dong C, Zhang H, Li L, Tempel W, Loppnau P, Min J (2018) Molecular basis of GID4-mediated recognition of degrons for the Pro/N-end rule pathway. *Nat Chem Biol* 14: 466–473
- Dong C, Chen S-J, Melnykov A, Weirich S, Sun K, Jeltsch A, Varshavsky A, Min J (2020) Recognition of nonproline N-terminal residues by the Pro/N-degron pathway. *Proc Natl Acad Sci USA* 117: 14158–14167
- Duda DM, Borg LA, Scott DC, Hunt HW, Hammel M, Schulman BA (2008) Structural insights into NEDD8 activation of cullin-RING ligases: conformational control of conjugation. *Cell* 134: 995–1006
- Gao J, Aksoy BA, Dogrusoz U, Dresdner G, Gross B, Sumer SO, Sun Y, Jacobsen A, Sinha R, Larsson E et al (2013) Integrative analysis of complex cancer genomics and clinical profiles using the cBioPortal. *Science Signaling* 6: 1–20
- Gerlitz G, Darhin E, Giorgio G, Franco B, Reiner O (2005) Novel functional features of the LIS-H domain: role in protein dimerization, half-life and cellular localization. *Cell Cycle* 4: 1632–1640
- Her L-S, Mao S-H, Chang C-Y, Cheng P-H, Chang Y-F, Yang H-I, Chen C-M, Yang S-H (2017) miR-196a enhances neuronal morphology through suppressing RANBP10 to provide neuroprotection in Huntington’s disease. *Theranostics* 7: 2452–2462
- Heusel M, Bludau I, Rosenberger G, Hafen R, Frank M, Banaei Esfahani A, Drogen A, Collins BC, Gstaiger M, Aebersold R (2019) Complex-centric proteome profiling by SEC-SWATH-MS. *Mol Syst Biol* 15: e8438
- Higa LA, Wu M, Ye T, Kobayashi R, Sun H, Zhang H (2006) CUL4-DDB1 ubiquitin ligase interacts with multiple WD40-repeat proteins and regulates histone methylation. *Nat Cell Biol* 8: 1277–1283
- Hong SK, Kim K-H, Song EJ, Kim EE (2016) Structural basis for the interaction between the IUS-SPRY domain of RanBPM and DDX-4 in germ cell development. *J Mol Biol* 428: 4330–4344
- Huber AH, Nelson WJ, Weis WI (1997) Three-dimensional structure of the armadillo repeat region of beta-catenin. *Cell* 90: 871–882
- Jiang G, Yang D, Wang L, Zhang X, Xu H, Miao Y, Wang E, Zhang Y (2015a) A novel biomarker ARMC8 promotes the malignant progression of ovarian cancer. *Hum Pathol* 46: 1471–1479
- Jiang G, Zhang Y, Zhang X, Fan C, Wang L, Xu H, Yu J, Wang E (2015b) ARMC8 indicates aggressive colon cancers and promotes invasiveness and migration of colon cancer cells. *Tumor Biol* 36: 9005–9013
- Jiang F, Shi Y, Lu H, Li G (2016) Armadillo repeat-containing protein 8 (ARMC8) silencing inhibits proliferation and invasion in osteosarcoma cells. *Oncol Res* 24: 381–389
- Khosravi R, Maya R, Gottlieb T, Oren M, Shiloh Y, Shkedy D (1999) Rapid ATM-dependent phosphorylation of MDM2 precedes p53 accumulation in response to DNA damage. *PNAS* 96: 14973–14977
- Kobayashi N, Yang J, Ueda A, Suzuki T, Tomaru K, Takeno M, Okuda K, Ishigatsubo Y (2007) RanBPM, Muskelein, p48EMLP, p44CTLH, and the armadillo-repeat proteins ARMC8 α and ARMC8 β are components of the CTLH complex. *Gene* 396: 236–247
- Kong K-YE, Fischer B, Meurer M, Kats I, Li Z, Rühle F, Barry JD, Kirrmaier D, Chevyreva V, Luis B-JS et al (2021) Timer-based proteomic profiling of the ubiquitin-proteasome system reveals a substrate receptor of the GID ubiquitin ligase. *Mol Cell* 81: 2460–2476.e11
- Lampert F, Stafa D, Goga A, Soste MV, Gilberto S, Olieric N, Picotti P, Stoffel M, Peter M (2018) The multi-subunit GID/CTLH E3 ubiquitin ligase promotes cell proliferation and targets the transcription factor Hbp1 for degradation. *Elife* 7: 1–23
- Leitner A, Reischl R, Walzthoeni T, Herzog F, Bohn S, Förster F, Aebersold R (2012) Expanding the chemical cross-linking toolbox by the use of multiple proteases and enrichment by size exclusion chromatography. *Mol Cell Proteomics* 11: 014126–1–014126–11
- Leitner A, Walzthoeni T, Aebersold R (2013) Lysine-specific chemical cross-linking of protein complexes and identification of cross-linking sites using LC-MS/MS and the xQuest/xProphet software pipeline. *Nat Protoc* 9: 120–137
- Leitner A, Joachimiak LA, Unverdorben P, Walzthoeni T, Frydman J, Förster F, Aebersold R (2014) Chemical cross-linking/mass spectrometry targeting

- acidic residues in proteins and protein complexes. *Proc Natl Acad Sci USA* 111: 9455–9460
- Levkowitz G, Waterman H, Ettenberg SA, Katz M, Tsygankov AY, Alroy I, Lavi S, Iwai K, Reiss Y, Ciechanover A *et al* (1999) Ubiquitin ligase activity and tyrosine phosphorylation underlie suppression of growth factor signaling by c-Cbl/Sli-1. *Mol Cell* 4: 1029–1040
- Li X, Mooney P, Zheng S, Booth CR, Braunfeld MB, Gubbens S, Agard DA, Cheng Y (2013) Electron counting and beam-induced motion correction enable near-atomic-resolution single-particle cryo-EM. *Nat Methods* 10: 584–590
- Liang X, Men Q-L, Li Y-W, Li H-C, Chong T, Li Z-L (2016) Silencing of armadillo repeat-containing protein 8 (ARMC8) inhibits TGF. *Oncol Res* 25: 99–105
- Maitland MER, Onea G, Chiasson CA, Wang XU, Ma J, Moor SE, Barber KR, Lajoie GA, Shaw GS, Schild-Poulter C (2019) The mammalian CTLH complex is an E3 ubiquitin ligase that targets its subunit muskulin for degradation. *Sci Rep* 9: 1–14
- Mallik S, Kundu S (2018) Topology and oligomerization of mono- and oligomeric proteins regulate their half-lives in the cell. *Structure* 26: 869–878
- Melnykov A, Chen S-J, Varshavsky A (2019) Gid10 as an alternative N-recognin of the Pro/N-degron pathway. *Proc Natl Acad Sci USA* 116: 15914–15923
- Menssen R, Bui K, Wolf DH (2018) Regulation of the Gid ubiquitin ligase recognition subunit Gid4. *FEBS Lett* 592: 3286–3294
- Mezulis S, Yates CM, Wass MN, Sternberg MJE, Kelley LA (2015) The Phyre2 web portal for protein modeling, prediction and analysis. *Nat Protoc* 10: 845–858
- Mohamed WI, Schenk AD, Kempf G, Cavadini S, Basters A, Potenza A, Rahman WA, Rabl J, Reichenmeier K, Thomä NH (2021) The CRL4^{DCAF3} cullin-RING ubiquitin ligase is activated following a switch in oligomerization state. *EMBO J* e108008
- Mohammadi A, Tschanz A, Leitner A (2021) Expanding the cross-link coverage of a carboxyl-group specific chemical cross-linking strategy for structural proteomics applications. *Anal Chem* 93: 1944–1950
- Nakatsukasa K, Nishimura T, Byrne SD, Okamoto M, Takahashi-Nakaguchi A, Chibana H, Okumura F, Kamura T (2015) The ubiquitin ligase SCFUcc1 acts as a metabolic switch for the glyoxylate cycle. *Mol Cell* 59: 22–34
- Nassan M, Li Q, Croarkin PE, Chen W, Colby CL, Veldic M, McElroy SL, Jenkins GD, Ryu E, Cunningham JM *et al* (2017) A genome wide association study suggests the association of muskulin with early onset bipolar disorder. Implications for a GABAergic epileptogenic neurogenesis model. *J Affect Disord* 208: 120–129
- Perez-Riverol Y, Csordas A, Bai J, Bernal-Llinares M, Hewapathirana S, Kundu DJ, Inuganti A, Griss J, Mayer G, Eisenacher M *et al* (2019) The PRIDE database and related tools and resources in 2019: improving support for quantification data. *Nucleic Acids Res* 47: D442–D450
- Pettersen EF, Goddard TD, Huang CC, Couch GS, Greenblatt DM, Meng EC, Ferrin TE (2004) UCSF Chimera: a visualization system for exploratory research and analysis. *J Comput Chem* 25: 1605–1612
- Pfirrmann T, Villavicencio-Lorini P, Subudhi AK, Menssen R, Wolf DH, Hollemann T (2015) RMND5 from *Xenopus laevis* is an E3 ubiquitin-ligase and functions in early embryonic forebrain development. *PLoS One* 10: e0120342
- Pierce NW, Lee JE, Liu X, Sweredoski MJ, Graham RLJ, Larimore EA, Rome M, Zheng N, Clurman BE, Hess S *et al* (2013) Cand1 promotes assembly of new SCF complexes through dynamic exchange of F box proteins. *Cell* 153: 206–215
- Punjani A, Rubinstein JL, Fleet DJ, Brubaker MA (2017) cryoSPARC: algorithms for rapid unsupervised cryo-EM structure determination. *Nat Methods* 14: 290–296
- Puverel S, Barrick C, Dolci S, Coppola V, Tessarollo L (2011) RanBPM is essential for mouse spermatogenesis and oogenesis. *Development* 138: 2511–2521
- Qiao S, Langlois CR, Chrustowicz J, Sherpa D, Karayel O, Hansen FM, Beier V, von Gronau S, Bollschweiler D, Schäfer T *et al* (2019) Interconversion between anticipatory and active GID E3 ubiquitin ligase conformations via metabolically driven substrate receptor assembly. *Mol Cell* 77: 150–163
- Sant O, Pfirrmann T, Braun B, Juretschke J, Kimmig P, Scheel H, Hofmann K, Thumm M, Wolf DH (2008) The yeast GID complex, a novel ubiquitin ligase (E3) involved in the regulation of carbohydrate metabolism. *Mol Biol Cell* 19: 3323–3333
- Scheres SHW (2016) Processing of structurally heterogeneous Cryo-EM Data in RELION. *Methods Enzymol* 579: 125–157
- Sherpa D, Chrustowicz J, Qiao S, Langlois CR, Hehl LA, Gottemukkala KV, Hansen FM, Karayel O, von Gronau S, Prabu JR *et al* (2021) GID E3 ligase supramolecular chelate assembly configures multipronged ubiquitin targeting of an oligomeric metabolic enzyme. *Mol Cell* 81: 2445–2459.e13
- Skraban CM, Wells CF, Markose P, Cho MT, Nesbitt AI, Au PYB, Begtrup A, Bernat JA, Bird LM, Cao K *et al* (2017) WDR26 haploinsufficiency causes a recognizable syndrome of intellectual disability, seizures, abnormal gait, and distinctive facial features. *Am J Hum Genet* 101: 139–148
- Stark H (2010) GraFix: stabilization of fragile macromolecular complexes for single particle Cryo-EM. *Methods Enzymol* 481: 109–126
- Tomaru K, Ueda A, Suzuki T, Kobayashi N, Yang J, Yamamoto M, Takeno M, Kaneko T, Ishigatsubo Y (2010) Armadillo repeat containing 8 α binds to HRS and promotes HRS interaction with ubiquitinated proteins. *Open Biochem J* 4: 1–8
- Wagner T, Merino F, Stabrin M, Moriya T, Antoni C, Apelbaum A, Hagel P, Sitsel O, Raisch T, Prumbaum D *et al* (2019) SPHIRE-crYOLO is a fast and accurate fully automated particle picker for cryo-EM. *Commun Biol* 2: 1–13
- Walzthoeni T, Claassen M, Leitner A, Herzog F, Bohn S, Förster F, Beck M, Aebersold R (2012) False discovery rate estimation for cross-linked peptides identified by mass spectrometry. *Nat Methods* 9: 901–903
- Waterhouse AM, Procter JB, Martin DMA, Clamp M, Barton GJ (2009) Jalview Version 2—a multiple sequence alignment editor and analysis workbench. *Bioinformatics* 25: 1189–1191
- Woo JA, Boggess T, Uhlar C, Wang X, Khan H, Cappos G, Joly-Amado A, De Narvaez E, Majid S, Minamide LS *et al* (2015) RanBP9 at the intersection between cofilin and $\alpha\beta$ pathologies: rescue of neurodegenerative changes by RanBP9 reduction. *Cell Death Dis* 6: 1–14
- Xie C, Jiang G, Fan C, Zhang X, Zhang Y, Miao Y, Lin X, Wu J, Wang L, Liu Y *et al* (2014) ARMC8 α promotes proliferation and invasion of non-small cell lung cancer cells by activating the canonical Wnt signaling pathway. *Tumour Biol* 35: 8903–8911
- Zhang K (2016) Gctf: Real-time CTF determination and correction. *J Struct Biol* 193: 1–12
- Zhao Y, Peng S, Jia C, Xu F, Xu Y, Dai C (2016) Armc8 regulates the invasive ability of hepatocellular carcinoma through E-cadherin/catenin complex. *Tumor Biol* 37: 11219–11224
- Zhou D, Zhang W, Wang Y, Chen L, Luan J (2016) ARMC8: a potential diagnostic and therapeutic target for cancers—reply. *Hum Pathol* 54: 201–202
- Zhu Q, Luo Z, Lu G, Gui F, Wu J, Li F, Ni Y (2018) LncRNA FBP5P3/miR-589-5p/ZMYND19 axis contributes to hepatocellular carcinoma cell proliferation, migration and invasion. *Biochem Biophys Res Comm* 498: 551–558



License: This is an open access article under the terms of the Creative Commons Attribution-NonCommercial-NoDeriv License, which permits use and distribution in any medium, provided the original work is properly cited, the use is non-commercial and no modifications or adaptations are made.